Results in Engineering 30 (2026) 110554

Contents lists available at ScienceDirect

Results in Engineering

journal homepage: www.sciencedirect.com/journal/results-in-engineering

# Additively manufactured maraging steel for electrical machines: Magnetic characterization and PMSM prototype

Jan Kaska [a,*], Tomáš Paveza [b], Zdeněk Frank [b], Lukáš Sobotka [b], Paavo Rasilo [a], Roman Pechánek [b]

[a] Electrical Engineering Unit, Tampere University, Korkeakoulunkatu 3, Tampere, 33720, Finland
[b] Department of Power Electronics and Machines, University of West Bohemia, Univerzitní 2732/8, Pilsen, 30100, Czech Republic

ARTICLE INFO

*Keywords:*
Additive manufacturing
Electrical machines
Iron loss
Magnetic material
Maraging steel
Permanent magnet synchronous motor

ABSTRACT

Additive manufacturing offers many opportunities for electrical machine applications, including new cooling structures, integrated channels, high fill factor windings, and novel magnetic cores. Although many materials for magnetic cores have been successfully printed, challenges often include a complex search for processing parameters and high iron loss. The primary objective of this study is the magnetic characterization of maraging steel, a material commonly available in the portfolios of metal additive manufacturing systems, with the aim of assessing its suitability for electrical machine applications. The material is first characterized magnetically, and a loss reduction method is proposed. To demonstrate its applicability, a permanent magnet synchronous machine is designed and experimentally evaluated using both metal and polymer additive manufacturing. Although the machine shows lower efficiency than conventional machines, the material still shows potential for applications where high iron loss is not too limiting.

## 1. Introduction

Although additive manufacturing (AM) is already widely used in mechanical and structural engineering, it is still not fully developed for electrical machines and electromechanical actuators. Yet, it offers many potential benefits, such as advanced cooling with integrated channels, printed windings with high fill factors, custom permanent magnets, and innovative magnetic core designs, especially for axial or transverse flux machines. Additive manufacturing also enables multiple separate machine components to be combined into one, and allows the use of functional anisotropy, whether mechanical or magnetic.

The literature reports numerous successfully printed magnetic core materials, ranging from silicon steels such as FeSi3 [1,2], FeSi4.5 [3], FeSi6 [4], and FeSi9 [5], to permalloys [6,7], nanocrystalline and amorphous materials [8–10], as well as promising new high-entropy alloys [11]. Printed materials often exhibit magnetic and mechanical anisotropies, and heat treatment is required to improve magnetic properties. But even then, these materials often have higher coercivity, lower maximum permeability, and greater losses than their conventional counterparts produced using highly refined manufacturing methods.

Magnetic alloys are not the primary focus of printer manufacturers, meaning they are usually not included in printer material portfolios. Therefore, suitable processing parameters and post-processing must be found, which can be particularly challenging for fragile materials such as FeSi9 or amorphous alloys. Another problem is iron loss, especially in silicon steels, which are commonly used as stacks of electrically insulated sheets (lamination). However, printing individual sheets is not beneficial, and there is also a risk of warping due to residual stress, and the sheet surfaces may suffer from high roughness [12].

Although the material examined in this study, maraging steel, is not a common magnetic material, it is a ferromagnetic material found in most powder bed fusion printer vendors' portfolios and, therefore, a common choice for early experiments with AM of actuators and electrical machines. Examples might be the synchronous reluctance rotor prototype in [13], a switched reluctance rotor in [14], or a simple stator in [15]. However, none of these studies examines the properties of this material in detail or sufficiently evaluates the effectiveness of the electric machine.

The primary objective of this study is to characterize the magnetic properties of additively manufactured maraging steel. Secondary objectives are (i) to propose a suitable iron-loss reduction technique and (ii) to design and experimentally evaluate a prototype permanent magnet synchronous machine.

* Corresponding author.
*E-mail address:* jan.kaska@tuni.fi (J. Kaska).

https://doi.org/10.1016/j.rineng.2026.110554
Received 26 January 2026; Received in revised form 27 March 2026; Accepted 14 April 2026
Available online 15 April 2026

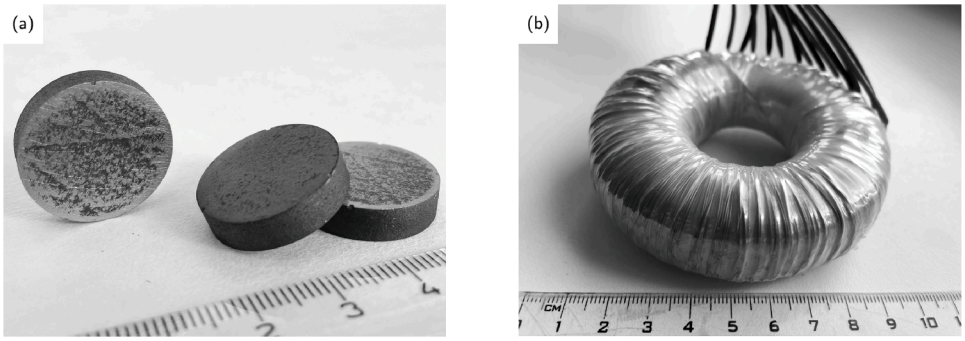


**Fig. 1.** (a) Cylindrical samples; (b) Toroidal core with winding.

## 2. Material characterization

The material selected for this study is maraging steel MS1 supplied by EOS GmbH. The composition of the powder corresponds to the US classification 18Ni-300, European 1.2709, and German X3NiCoMoTi18-9-5, and is shown in detail in Table 1. All samples in this study are printed using a powder bed fusion printer EOS M290 with the manufacturer's default processing parameters for this material: laser power 285 W, scanning speed 960 $\mathrm{mm \cdot s^{-1}}$, layer thickness 40 $\mu$m, and hatch distance 110 $\mu$m. Nitrogen is used as the protective atmosphere.

**Table 1**
Powder chemical composition.

| Element | Ni | Co | Mo | Ti | Al |
|---|---|---|---|---|---|
| Weight % | 17-19 | 8.5-9.5 | 4.5-5.2 | 0.6-0.8 | 0.05-0.15 |

Many papers deal with the mechanical properties of printed maraging steel [16,17], but much fewer address its magnetic properties. Study [18] investigates the effect of build orientation on the magnetic properties of toroidal transformer cores, while [19] evaluates the magnetic properties of MS1 powder, finding that heat treatment only marginally enhances its soft magnetic behavior. Both studies show that the material is predominantly ferromagnetic, and its coercivity classifies it as a semi-hard magnetic material.

The overview of possible rotor materials [20] lists maraging steel as a potential candidate for high-speed motor applications requiring high tensile strength, although it should be noted that specialized materials with high mechanical strength and low coercivity have been developed, such as [21]. In addition, thanks to its high nickel content, the maraging steel has relatively high electrical resistivity.

### 2.1. Samples and methods

Magnetic properties are measured using two types of samples. Quasi-stationary hysteresis loops are obtained using eight cylindrical samples with a radius of 20.5 mm and a height of 5.5 mm, shown in Fig. 1 (a), using a *Hystograph HG 200* from *Brockhaus GmbH & Co. KG* - a closed-circuit measurement device for measuring semi-hard and hard magnetic materials. For this measurement, the surfaces in contact with the measuring poles of the device must be parallel; otherwise, the measurement will be distorted by an air gap. The top surface of cylindrical samples is thus first sanded, and the bottom surface is then aligned using a lathe. Small notches are made on the edges to identify individual samples.

Dynamic iron loss is measured using three toroidal cores (one as-built and two heat-treated) with an outer diameter of 80 mm, an inner diameter of 60 mm, and a height of 10 mm. Both the top and bottom surfaces of the cores are aligned using a lathe, and the build direction is parallel to the cylindrical or toroidal axis of the samples. The heights and diameters of the manufactured samples were measured multiple times at several locations and averaged.

The measuring device is *MPG 200* from *Brockhaus GmbH & Co. KG*, which is able to control the input current to ensure that the magnetic induction remains harmonic, as required by the EN IEC 60404-6 standard. A wound toroidal core is shown in Fig. 1 (b). As the material is semi-hard and thus requires a high input power, the winding has 1800 turns on the primary and secondary windings, with several taps provided to enable measurements with a limited power supply at higher frequencies. The taps are always connected so that the toroid is magnetized along its entire length.

### 2.2. Quasi-stationary properties

Prior to measurements, all eight cylindrical samples are demagnetized, and the curves are then measured up to magnetic saturation. All measured curves are smoothed using the moving average method, centered, following the methodology presented in [22,23], and sampled to a new grid of applied field values $H$. This allows computation of a mean hysteresis loop. The mean loop and its standard deviation for the eight samples are shown in Fig. 2.

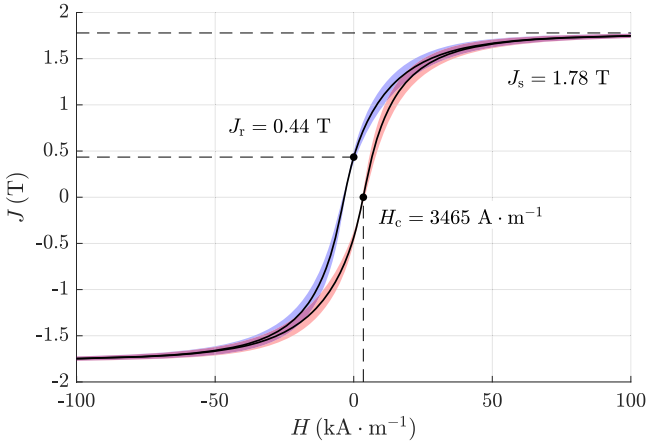


**Fig. 2.** Mean hysteresis loop (black line) with standard deviation of $J$ (blue and red areas); Coercivity $H_c$, saturation polarization $J_s$, and remanent polarization $J_r$ are marked. (For interpretation of the references to colour in this figure legend, the reader is referred to the web version of this article.)

The standard deviation for the ascending branch is marked in blue, and for the descending branch in red. These correspond to the standard deviations of the magnetic polarization $J$ for each point of the applied field $H$. This shows that the variation among the curves lies primarily in their steepness $\mathrm{d}J/\mathrm{d}H$. The mean values of coercivity $H_c$, saturation polarization $J_s$, and remanent polarization $J_r$ are indicated.

The trend is also evident in Table 2, presenting the mean values, standard deviations and confidence intervals for the main parameters of the hysteresis loop: coercivity $H_c$, saturation polarization $J_s$ and its

**Table 2**
Main parameters of the hysteresis loop.

| | $H_c$ (kA · m$^{-1}$) | $J_s$ (T) | $\mu_r$ ($1 \times 10^1$) | $J_r$ (T $\times 10^{-1}$) | $H_s$ (kA · m$^{-1}$ $\times 10^2$) |
|---|---|---|---|---|---|
| Mean±SD | $3.47 \pm 0.1$ | $1.78 \pm 0.01$ | $8.79 \pm 1.37$ | $4.35 \pm 0.62$ | $3.07 \pm 0.12$ |
| 95% CI | [3.38, 3.55] | [1.77, 1.79] | [7.64, 9.93] | [3.83, 4.86] | [2.97, 3.17] |

corresponding applied field $H_s$, remanent polarization $J_r$, and maximum relative permeability $\mu_r$, calculated as the maximum of $B/H$ of the initial magnetization curves. Among these parameters, $J_r$ and $\mu_r$ show the highest standard deviation.

As expected, MS1 is a magnetically semi-hard material. When compared to a material such as silicon steel FeSi 2-3.5%, commonly used in electrical machines, the main differences are high coercivity $H_c$, which is reported as 8-100 A · m$^{-1}$ for FeSi, and low remanent polarization (0.8-1.2 T for FeSi), which is also associated with low relative permeability. This means that either a larger volume of material or higher input power is required to achieve the same magnetic flux through the magnetic core as with silicon steels.

The measured initial magnetization curves of all eight cylindrical samples are used to fit the $BH$ curve with a double Langevin function

$$B = \mu_0 H + \sum_{i=1}^{2} J_s^i \left( \coth\left(\frac{H}{H_0^i}\right) - \frac{H_0^i}{H} \right), \tag{1}$$

where $J_s^i$ and $H_0^i$ are the unknown parameters and $\mu_0$ is vacuum permeability. The coefficients fitted using nonlinear least squares are shown in Table 3 along with the confidence intervals (95%) obtained via bootstrap resampling, as in all the following models. The coefficient of determination is 0.9954. In the limit of an infinitely large applied field $H$, the sum of $J_s^1$ and $J_s^2$ corresponds to the saturation polarization $J_s$. This is true, since $J_s^1 + J_s^2 = 1.79$ T, which is close to 1.78 T in Table 2. The resulting model, together with the measured data, is shown in Fig. 3. The measured curves again show the greatest variance at the knee of the curve.

**Table 3**
Magnetization curve regression coefficients.

| | $J_s^1$ (T $\times 10^{-1}$) | $J_s^2$ (T) | $H_0^1$ (kA · m$^{-1}$ $\times 10^1$) | $H_0^2$ (kA · m$^{-1}$) |
|---|---|---|---|---|
| LS estimate | −2.81 | 2.07 | 3.70 | 7.12 |
| 95% CI | −[2.56, 3.02] | [2.05, 2.09] | [3.70, 3.70] | [6.95, 7.24] |

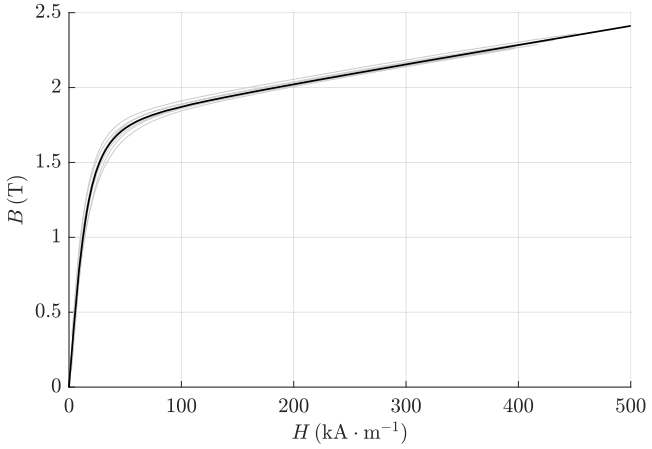


**Fig. 3.** Measured magnetization curves (grey) fitted with double Langevin model (black).

The double Lagnevin function has two more parameters than the single version and can therefore better represent the shape of the anhysteretic curves [24]. This approach is used for magnetic models such as [25,26]. This function can also be used to fit the magnetization curves that do not have a pronounced initial knee, as is the case with this material.

The measured quasi-stationary curves are further used to determine the gravimetric hysteresis energy loss density $W_h$, as the area of the hysteresis loop measured for several values of maximum magnetic induction. The data are then interpolated using Steinmetz's formula

$$W_h = w_1 B^{w_2}, \tag{2}$$

where the exponent $w_2$ typically ranges from 1.2 to 2. The optimal least-squares parameters are shown in Table 4 along with confidence intervals. Fig. 4 then shows the data points measured on the cylindrical specimens used as data for the model, as well as the loss obtained from dynamic measurements of the toroidal core. It is evident that once a certain value of magnetic induction $B$ is reached, the trend begins to diverge, as discussed in [27]. Beyond this point, the area of the hysteresis loop that determines the loss increases only slightly with increasing magnetic induction. The model's validity is therefore limited to approximately 1.7 T.

**Table 4**
Hysteresis loss regression coefficients.

| | $w_1$ (J · kg$^{-1}$ · T$^{-w_2}$) | $w_2$ (–) |
|---|---|---|
| LS estimate | 0.81 | 1.55 |
| 95% CI | [0.70, 1.39] | [0.75, 1.61] |

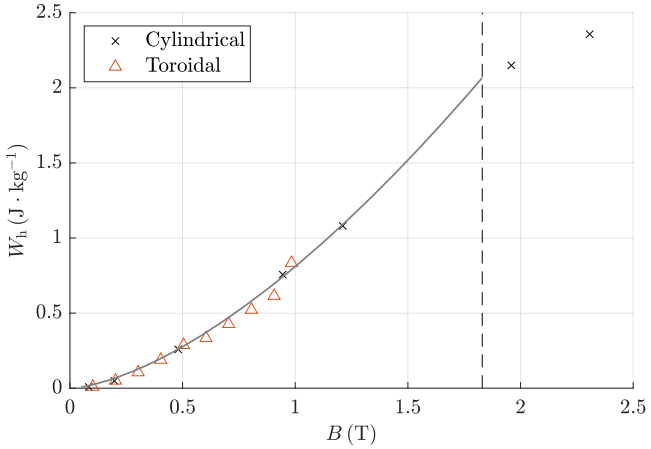


**Fig. 4.** Measured hysteresis loss from cylindrical (cross marker) and toroidal (triangle marker) samples and fitted curve (solid line).

### 2.3. Dynamic properties

The measurements of specific iron loss are performed using a wound toroidal core for frequencies from 20 to 800 Hz and magnetic inductions ranging from 0.1 to 1.1 T in increments of 0.1 T. However, not all combinations are measured due to power supply limitations. The measured gravimetric power loss density $P$ is again fitted using Steinmetz's formula

$$P = w_1 B^{w_2} f^{w_3}, \tag{3}$$

with optimal least-squares parameters shown in Table 5 along with confidence intervals, the coefficient of determination is then 0.9982.

The Fig. 5 shows that although the coefficient of determination is high, the trend of loss is not captured perfectly; errors occur mostly for small values of magnetic induction and lower frequencies. The loss is approximately two orders of magnitude higher than, for example,

M350-50A electrical steel. This is due to the high hysteresis loss of the semi-hard magnetic material and to the fact that these measurements are performed on a bulk toroidal core without any iron loss reduction. Fig. 6 then shows swelling of hysteresis loops for 0.5 T and increasing frequency.

**Table 5**
Gravimetric power loss density regression coefficients.

| | $w_1$ $(\mathrm{W \cdot kg^{-1} \cdot T^{-w_2} \cdot Hz^{-w_3}})$ | $w_2$ (−) | $w_3$ (−) |
|---|---|---|---|
| LS estimate | 0.24 | 2.07 | 1.47 |
| 95% CI | [0.21, 0.3] | [1.98, 2.13] | [1.42, 1.51] |

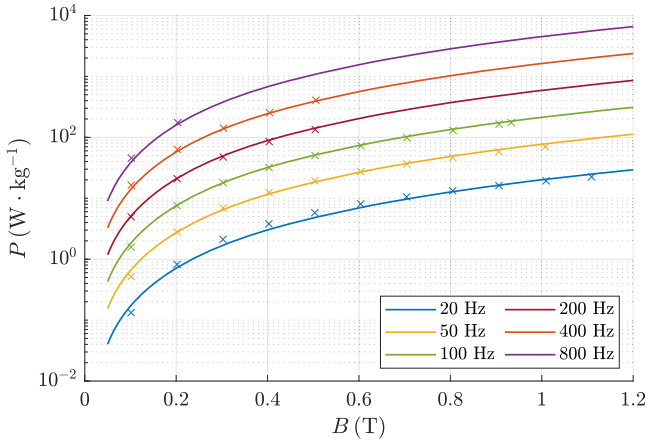


**Fig. 5.** Measured specific iron loss (cross marker) fitted with Steinmetz's formula (solid lines) for multiple frequencies.

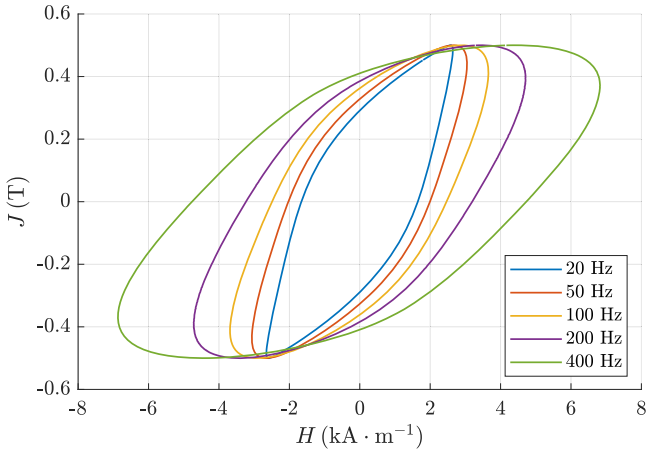


**Fig. 6.** Swelling of hysteresis loop with rising frequency.

### 2.4. Heat treatment

The aim of heat treatment is to bring the properties of maraging steel closer to those of conventional magnetically soft materials, i.e., to reduce coercivity, increase remanent polarization, and increase maximum relative permeability. Inspiration was drawn from studies such as [28], for silicon steels, where temperatures of around 1000 °C yield a significant improvement in soft magnetic properties.

The effect of heat treatment is tested using two processes, HT1 and HT2, recommended by the powder manufacturer to improve the mechanical properties of the maraging steel. The initial stage of both processes aims to relieve the material's internal stresses, while the second stage, also known as aging, involves the precipitation of intermetallic compounds. In this study, the aging stage is omitted. As shown in Fig. 7, HT1 process heats the samples to 820 °C with a one-hour dwell time, while HT2 uses a higher temperature of 940 °C and doubles the dwell time. Both treatments are carried out in a nitrogen protective atmosphere, and the samples are then furnace-cooled.

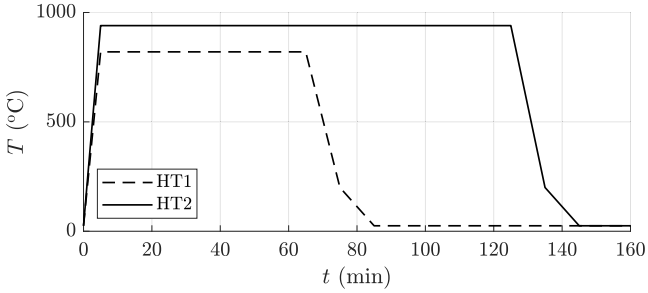


**Fig. 7.** Old (HT1) and new (HT2) heat treatment profiles.

The results of the treatments are summarized in Table 6. In general, the parameter changes observed in either process are not as pronounced as those reported for silicon steels. Heat treatment deteriorates the desired soft-magnetic properties in both cases by increasing the coercivity $H_c$ and reducing the remanent polarization $J_r$. On the positive side, there is an increase in saturation polarization $J_s$ and its shift towards lower values of the applied field $H_s$, but these changes are minimal. The relative permeability is not given, as its value has such a high standard deviation that it is difficult to compare meaningfully. However, since the greatest changes occur in the knee region of the curve, the $H_{1T}$ parameter was added, which corresponds to the value of the applied field for a magnetic polarization of 1 T. This parameter then exhibits the greatest change of all parameters for both HT1 and HT2.

The effect of heat treatment on the parameters is further evaluated using a paired *t*-test at a 5% significance level. Initially, the as-built and heat-treated states are compared separately for each heat-treatment condition ($n = 4$), yielding inconclusive results: approximately half of the parameters show differences that were not statistically significant. Subsequently, all as-built samples are compared with all heat-treated samples combined (HT1 and HT2, $n = 8$), resulting in statistically significant differences across all parameters. Effect sizes are quantified using Cohen's $d$, revealing large effects ($d > 1$) for all parameters, with the exception of $H_s$, which exhibited a smaller effect. It should be noted that

**Table 6**
Change in main parameters of the hysteresis loop after heat treatments.

| | | Mean±SD | | 95% CI | | % Change | |
|---|---|---|---|---|---|---|---|
| | | HT1 | HT2 | HT1 | HT2 | HT1 | HT2 |
| $H_c$ | $(\mathrm{kA \cdot m^{-1}})$ | $4.04 \pm 0.25$ | $3.55 \pm 0.09$ | [3.65, 4.43] | [3.41, 3.69] | +16.52 | +2.45 |
| $J_s$ | (T) | $1.80 \pm 0.01$ | $1.83 \pm 0.01$ | [1.78, 1.82] | [1.81, 1.84] | +1.27 | +2.74 |
| $J_r$ | $(\mathrm{T} \times 10^{-1})$ | $3.77 \pm 0.26$ | $3.41 \pm 0.19$ | [3.36, 4.17] | [3.10, 3.70] | −13.32 | −21.76 |
| $H_{1T}$ | $(\mathrm{kA \cdot m^{-1}} \times 10^1)$ | $1.32 \pm 0.13$ | $1.38 \pm 0.09$ | [1.12, 1.52] | [1.24, 1.52] | +65.53 | +58.84 |
| $H_s$ | $(\mathrm{kA \cdot m^{-1}} \times 10^2)$ | $3.01 \pm 0.12$ | $2.71 \pm 0.08$ | [2.82, 3.20] | [2.58, 2.84] | −1.85 | −11.68 |

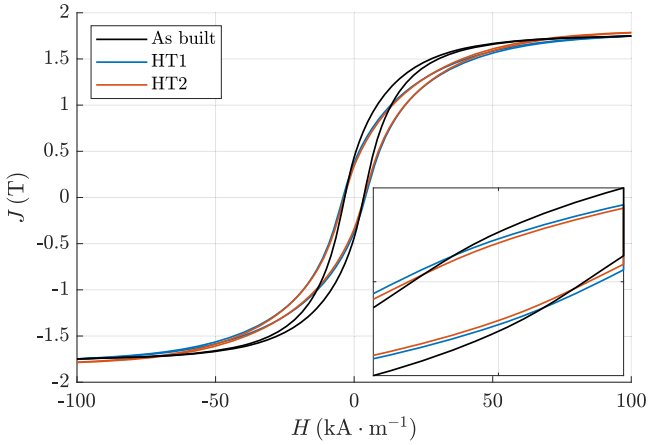


**Fig. 8.** Mean hysteresis loops before and after heat treatments.

the sample size is limited, and thus the statistical power of the individual tests is low. The lack of significance in some cases might therefore be attributed to the small sample size rather than the absence of an effect.

The as-built mean hysteresis loop and the mean curves after both heat treatment processes are shown in Fig. 8, with a detailed view of the region from -5 to 5 $\mathrm{kA \cdot m^{-1}}$. As for the specific iron loss, both processes reduce the loss for magnetic inductions above approximately 0.2 T. For example, at 1 T and 50 Hz, the loss of the as-built core is about 70 $\mathrm{W \cdot kg^{-1}}$, decreasing to 60 $\mathrm{W \cdot kg^{-1}}$ after HT2 and 50 $\mathrm{W \cdot kg^{-1}}$ after HT1. However, as with quasi-stationary magnetic properties, no significant change is observed as shown in Fig. 9. It should also be noted that the loss measurements are performed on three toroidal cores: one as-built and two with different heat treatments, HT1 and HT2. There may be other minor differences between these cores, so for a more thorough assessment, it would be advisable to measure loss on multiple heat-treated samples. It will also be appropriate to examine the microstructure of the samples before and after heat treatment.

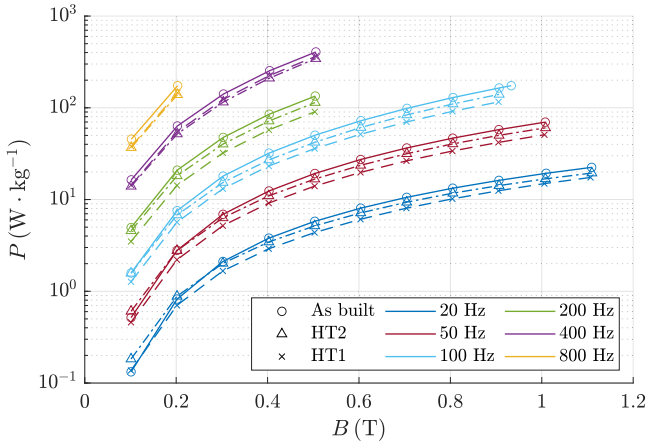


**Fig. 9.** Specific iron loss before and after heat treatments.

Changes in coercivity, and thus in hysteresis losses, are often linked to grain size, which increases during heat treatment in printed silicon steels [1]. In this case, however, it appears that different mechanisms are at work. The authors [29] show that the coercivity of maraging steel increases with heat treatment temperature to a maximum, followed by a decrease at higher temperatures, which corresponds to the behavior of HT1 and HT2. The authors attribute this to the growth of two types of austenite: para- and ferromagnetic. However, this is only a hypothesis that will need to be confirmed by further analysis.

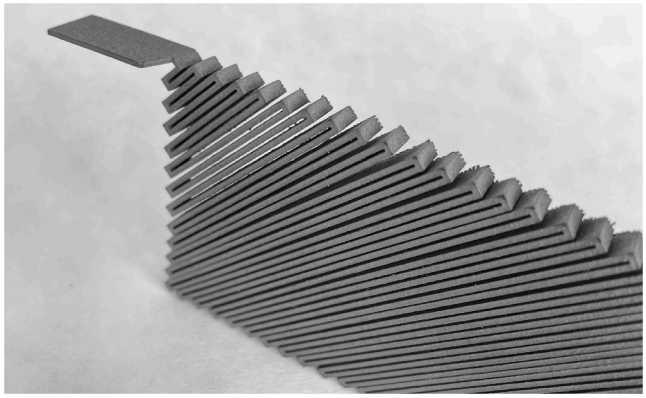

**Fig. 10.** Printed sample for electrical conductivity measurement.

### 2.5. Electrical conductivity

The electrical conductivity of maraging steel is measured using the sample shown in Fig. 10. First, the sample's resistance is measured using a four-wire method with *CROPICO Microohmmeter DO5000*, followed by a current conservation finite element simulation of the sample with conductivity set to one. By comparing the simulated resistivity and the measurement, the electrical conductivity of the material is calculated. There is a concern that the narrow gaps between the paths could be partly short-circuited by trapped powder or burrs. To address this, the gaps are cleaned with sandpaper, and the sample is stretched to check whether the resistance value changes.

The obtained conductivity is 1.41 $\mathrm{MS \cdot m^{-1}}$, corresponding to a resistivity of 71.2 $\mu\Omega \cdot$ cm. The resistivity is higher than that of FeSi3, which is about 45 $\mu\Omega \cdot$ cm, but slightly lower than that of FeSi6.5, which reaches about 82 $\mu\Omega \cdot$ cm. The high resistivity of the material is due to additives: nickel, cobalt, and molybdenum all increase the electrical resistivity of steel.

## 3. Iron loss reduction

The problem with maraging steel is its high iron loss. This includes hysteresis loss, which depends on the material composition and microstructure, and dynamic loss, which is usually mitigated by lamination. Several methods to reduce eddy current loss in AM parts are described in the literature, often based on the concept of lamination, such as [28,30], or [31]. Although this approach is functional, the stacking factor is reduced because the insulating gap between parallel walls is typically tenths of a millimetre, in contrast to the micrometer-thick insulation of electrical steel.

One way to increase the stacking factor is to print a folding pattern [32], which is then coated with insulation and compressed. Another approach is to print multiple parts that fit tightly together [33]. The insulating layers can also be printed directly using a multimaterial printer, as in [34]. The problem is that electrically insulating materials usually have different melting temperatures than magnetic materials, or they require a different type of laser. Study [35] suggests printing in an oxygen-rich atmosphere to form an oxidation layer on the deposited layers or printing two materials, one of which is subsequently converted into an insulating material by oxidation. It is also possible to modify the structure of the material using various geometric patterns, such as slits or maze patterns [36,37] or to exploit the natural brittleness of materials such as FeSi6 in a controlled manner [38].

For printing the PMSM machine, described in more detail in the following section, the concept of electrically insulated sheets is applied, aiming at the smallest possible gap between the parallel walls. The minimum gap is determined to be 0.25 mm. At this distance, wall sticking

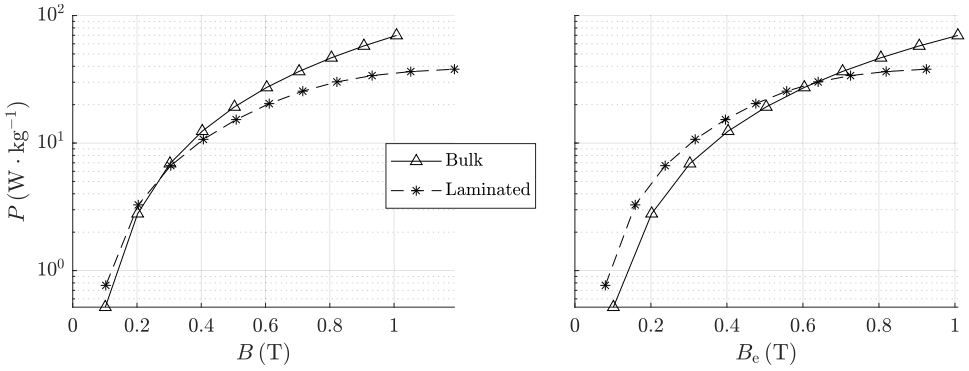


**Fig. 11.** Specific iron loss of bulk and laminated toroidal cores in relation to magnetic induction $B$ and effective induction $B_\mathrm{e}$.

is minimal, and the remaining powder can be removed. The wall is then 0.75 mm thick, yielding a stacking factor of 75 %.

Since this is a permanent magnet synchronous machine, it is sufficient to laminate only the rotor surface, where most of the losses occur. The stator segments are laminated in their entire volume, but since the walls must hold together, they are connected by narrow bridges. The bridges were designed primarily with regard to printability and warping during printing, and in such a way that the effectiveness of loss reduction would not be significantly compromised. Given the properties of printed maraging steel [39,40], it was assumed that mechanical strength would not be an issue even with narrow bridges.

Both stator and rotor segments are shown in Fig. 12. Computed tomography scans are performed on several segments to confirm that the gaps between the walls were indeed clean; these scans can be seen in Fig. 13. Except for a few spots, the gaps are clean, and the walls do not stick together.

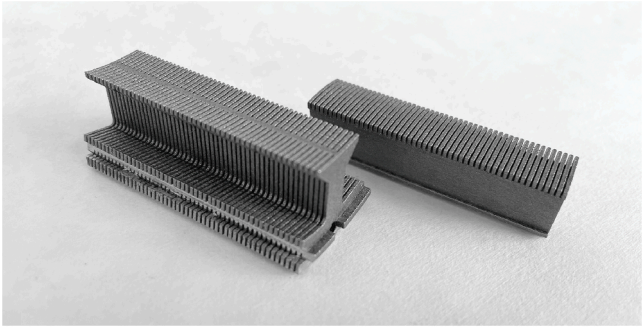

**Fig. 12.** Printed rotor and stator segments.

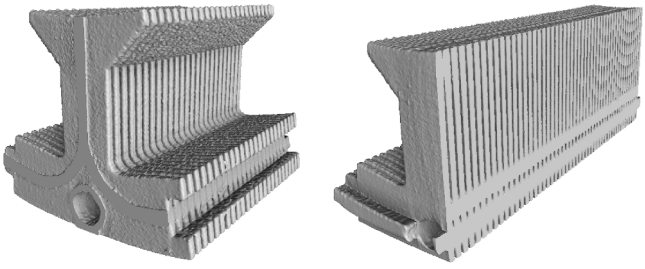

**Fig. 13.** Computed tomography scans of stator segment.

A toroidal core with the same stacking factor is also manufactured, and specific loss is measured. Two wall connection variants are tested, as shown in Fig. 14. Although finite element simulations indicate that the left variant should be approximately 10 % more effective, both cores yield identical results in actual measurements.

Fig. 11 then shows the specific iron loss compared to a bulk core at 50 Hz. When comparing loss, it is necessary to take into account the maximum magnetic induction, frequency, and stacking factor [41]. As the figure shows, if efficiency is evaluated in terms of the magnetic induction in the iron $B$, the reduction appears to be effective across the range of maximum inductions. However, if evaluated in terms of effective magnetic induction $B_\mathrm{e}$, the situation is different, and it is clear that for lower inductions associated with lower loss, it is more advantageous to use a bulk core. Effective magnetic induction $B_\mathrm{e}$ here means the average induction over the entire volume of the toroidal core (both iron and air gaps).

In both cases, however, it holds true that for 1 T and 50 Hz, lamination reduces loss by approximately 50 %. It should be noted that this still does not bring the loss close to conventional soft magnetic materials. Also, it cannot be automatically assumed that the loss reduction in the stator teeth will be as effective as in a toroidal core, since the magnetic flux paths are different and, for example, rotational loss also comes into play.

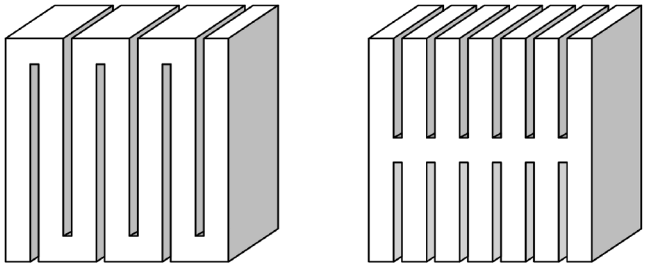

**Fig. 14.** Two variants of wall connections in toroidal core.

## 4. Additively manufactured PMSM

The prototype electric machine design is based on the cross-country electric motorcycle drive presented in studies [42,43]. The main parameters are listed in Table 7. The aim is to additively manufacture as many parts of the electric machine as possible. In addition to the stator and rotor parts, the frame, shaft, and bearing housing are also printed, this time using Nylon PA12 and a *SINTRATEC S2* printer. The only conventional parts are the N42 neodymium magnets, copper winding, bearings, and connecting elements.

The original machine design is modified to account for both the new materials and additive manufacturing. However, the original machine's main dimensions remain unchanged, as shown in Fig. 15. While rotor segments are now laminated on the surface, the original stator underwent more significant changes. It is divided into 18 segments for printability and to simplify winding, and the outer surfaces of the segments are flat to ensure easy removal from the printing platform and subse-

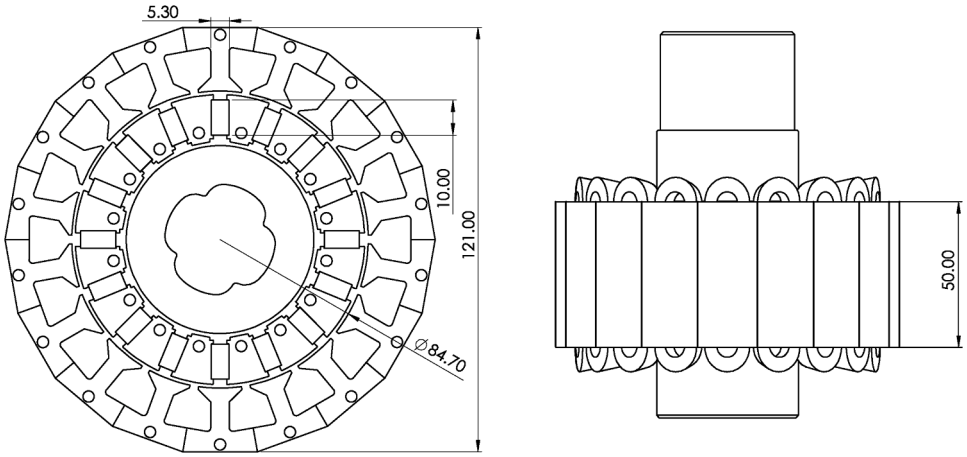


**Fig. 15.** Detailed machine dimensions (front and side view).

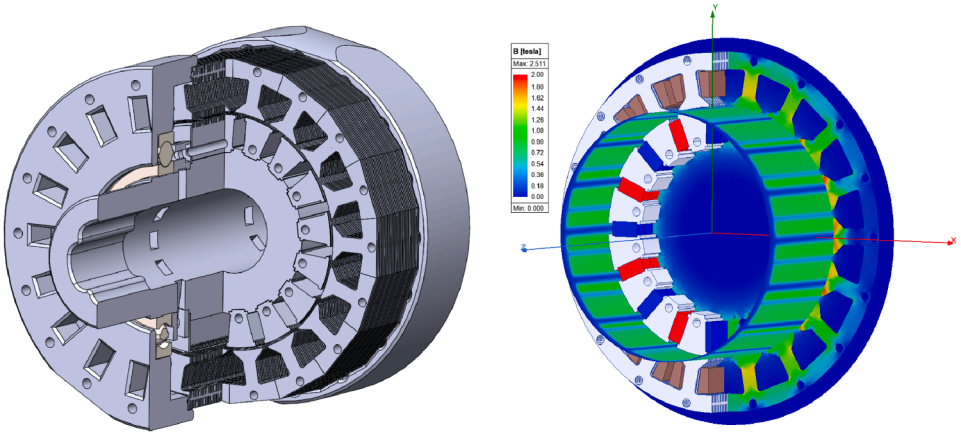

**Fig. 16.** 3D model of prototype machine (left); Magnetic induction in the cross-section and airgap (right).

**Table 7**
Parameters of the prototype PMSM machine.

| | |
|---|---|
| Number of slots per pole and phase | 3/9 |
| Number of poles | 16 |
| Rated speed | 750 rpm |
| Stator inner diameter | 84.7 mm |
| Air gap length | 1 mm |
| Number of turns in series | 180 |

quent machining. The air gap of the original machine is then increased from 0.8 mm to 1 mm due to concerns about the tolerances of the final assembly. The stator segments are then laminated along their entire length and held together by narrow bridges, as described in detail in the previous section. They feature holes and an interlocking mechanism to secure them into their final octadecagon shape. The segments are printed using the same processing parameters as the measurement samples in previous sections and are not heat-treated, as this did not bring any significant benefits to the magnetic properties.

The machine design is further verified using three-dimensional finite element analysis. The magnetic induction in the machine's cross-section and airgap is shown in Fig. 16, together with a model of the final design. The printed and wound machine with magnets installed is shown in Fig. 17. Since the original dimensions have been kept and an iron loss reduction strategy with a stacking factor of 75 % has been implemented, the proportion of stator core material in the machine is lower. Therefore, higher input power will be required to achieve the torque of the original machine.

### 4.1. Verification

Many studies of printed electrical machines conclude that the machines are functional, but their parameters are rarely verified. The aim of this section is therefore to determine the efficiency of an additively manufactured machine under various loads and speeds.

The machine is first measured in no-load and short-circuit conditions to identify the rated electrical parameters, namely the armature resistance at 20 °C, resulting in 0.316 Ω (mean of three phases), and the direct axis inductance, which is determined as 2.9 mH. The no-load voltage and the short-circuit current measured by the oscilloscope are shown in Fig. 18. The slightly different phase amplitudes in the figure indicate that the machine's airgap is not perfectly round. The problem lies in the interlocking of the individual rotor and stator segments. These locks had to be manually polished after printing, which resulted in uneven surfaces. For future prototypes, the locks will be simplified and will not require additional polishing.

The machine is measured as a generator using a resistive load, with the shafts of the prototype and the asynchronous motor connected via a torque sensor, as shown in Fig. 19. Measurements are taken at several speeds and power loads, always until the machine temperature stabilizes. The temperature is monitored by a sensor located in the stator winding. The measurements are taken at a constant room temperature of 25 °C without any external forced ventilation.

Table 8 shows the measured parameters, where $f$ is the frequency, $n$ is the rotor speed, $P$ is the resistive power load, $\tau$ is the torque, $T_w$ is the stator winding temperature, and $\eta$ is the efficiency. The rated speed was not reached due to high temperature, which could damage both

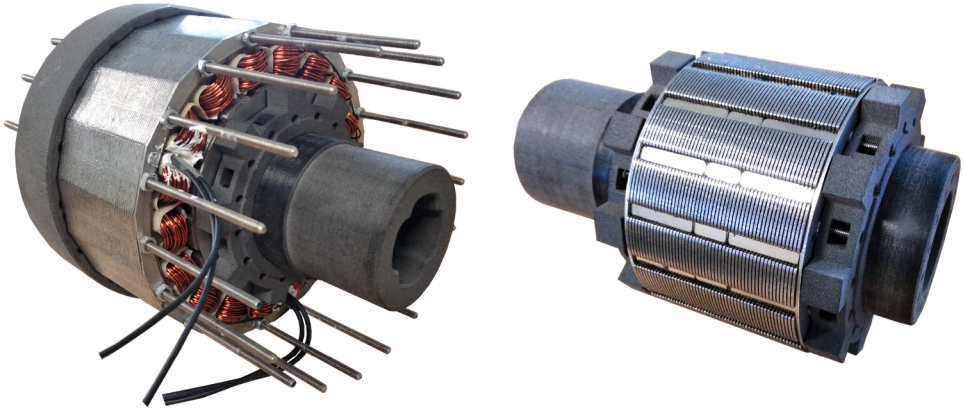

**Fig. 17.** Assembled prototype machine (left); Rotor with magnets installed (right).

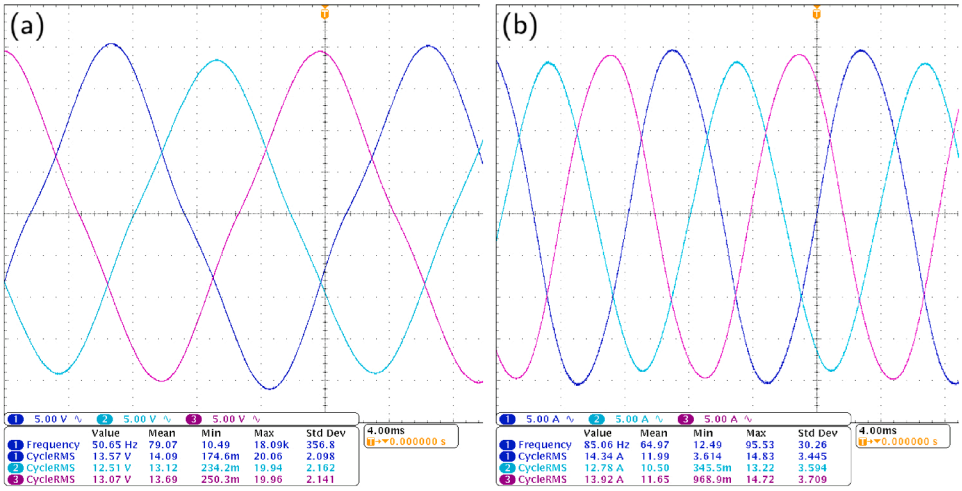


**Fig. 18.** (a) Voltage during the no-load measurement; (b) Current during the short-circuit measurement.

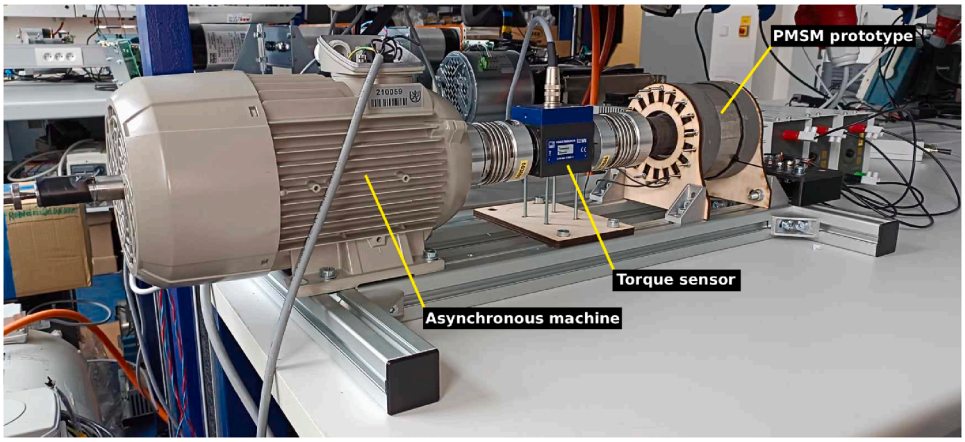


**Fig. 19.** Measurement configuration of the prototype PMSM.

the winding insulation and the nylon parts of the machine. It should be noted that the machine lacks a fan, and the nylon parts do not conduct heat well. There are no dedicated cooling fins, although the relatively wide lamination gaps help dissipate heat.

Fig. 20 then shows the dependence of the machine input power on the frequency at different stabilized temperatures denoted by colors. In general, it can be stated that the machine is functional, however, the higher required input power and greater losses compared to the original machine lead to significantly higher temperatures, a situation further complicated by factors such as the absence of a fan. In the future, it will be advisable to perform more detailed temperature measurements and thermal or fluid dynamics simulations to more clearly identify heat sources and design a efficient cooling system.

**Table 8**
Measured parameters of the machine.

| $f$ (Hz) | $n$ (rpm) | $P$ (W) | $\tau$ (Nm) | $T_w$ (°C) | $\eta$ (%) |
|---|---|---|---|---|---|
| 10 | 76 | 1.4 | 3.3 | 70 | 5.5 |
| 10 | 76 | 4.1 | 2.3 | 50 | 22.0 |
| 20 | 149 | 11.9 | 2.1 | 60 | 36.1 |
| 20 | 149 | 16.2 | 3.1 | 80 | 33.3 |
| 50 | 376 | 47.0 | 2.5 | 100 | 47.1 |
| 51 | 381 | 69.4 | 3.4 | 125 | 50.7 |
| 60 | 453 | 53.1 | 2.4 | 100 | 46.6 |
| 60 | 452 | 85.4 | 3.3 | 125 | 54.1 |

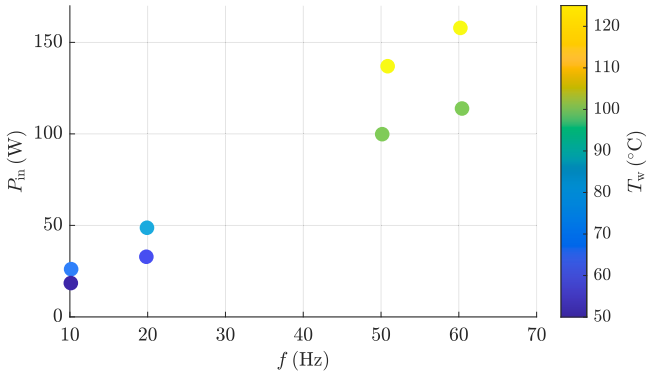


**Fig. 20.** Input power as a function of frequency and winding temperature.

## 5. Conclusions

The primary objective of this study was to characterize the magnetic properties of additively manufactured maraging steel as a magnetic core material for electrical machines. The magnetic characterization showed that maraging steel exhibits semi-hard magnetic behavior, with high coercivity, low maximum permeability, and iron losses significantly higher than those of conventional electrical steels. The heat treatments commonly used with additively manufactured silicon steels did not provide a significant improvement in the material's soft magnetic properties; however, further studies will be needed to investigate changes in the material's microstructure. Electrical conductivity measurements confirmed a relatively high resistivity, which is beneficial but, on its own, insufficient to reduce iron loss.

To address these limitations, an iron loss reduction strategy based on parallel walls separated by air gaps, similar to conventional lamination, was proposed and tested on a printed toroidal core. The results show that this approach leads to a significant reduction in total losses compared to bulk material, while preserving the advantages of additive manufacturing. Although the strategy was effective, material losses remain high compared to conventional soft magnetic materials. Results also show that it is necessary to carefully evaluate the trade-off between loss reduction and the stacking factor, taking into account the operating frequency and the maximum magnetic induction. To ensure printability and meet mechanical constraints, a stacking factor of approximately 75 % was selected.

Based on the measured material properties and the proposed loss reduction strategy, an additively manufactured permanent magnet synchronous machine was designed, built, and experimentally verified. Most of the machine parts were printed, using either maraging steel or nylon. The highest achieved efficiency was 54 %. Although the low efficiency is certainly partly due to imprecise assembly and manual winding, the main causes are increased winding losses due to higher current density and, above all, high iron losses, particularly in the stator. In the future, it would be beneficial to test other loss-reduction strategies that do not significantly reduce the stacking factor, as well as to test a printed rotor with a conventional stator.

Overall, the results show that while maraging steel is not competitive with conventional electrical steels, its widespread availability in metal additive manufacturing systems makes it a potential material for rapid prototyping and applications where iron loss is not the primary constraint.

## Declaration

During the preparation of this work, the authors used ChatGPT and Grammarly in order to improve readability and perform minor grammatical corrections. After using this tool/service, the authors reviewed and edited the content as needed and take full responsibility for the content of the publication.

## CRediT authorship contribution statement

**Jan Kaska:** Writing – original draft, Visualization, Methodology, Investigation, Data curation; **Tomáš Paveza:** Methodology, Investigation; **Zdeněk Frank:** Methodology, Investigation; **Lukáš Sobotka:** Methodology, Investigation; **Paavo Rasilo:** Writing – review & editing, Supervision; **Roman Pechánek:** Writing – review & editing, Supervision, Funding acquisition, Conceptualization.

## Data availability

Data will be made available on request.

## Declaration of competing interest

The authors declare that they have no known competing financial interests or personal relationships that could have appeared to influence the work reported in this paper.

## Acknowledgement

This work was supported by the Technology Agency of the Czech Republic under the project TA ČR NCK 2 CAMAT TN02000028 and the University of West Bohemia internal project SGS-2024-025 – Computational intelligence assisted design of electric and electronic devices.

## References

[1] S. Gao, H. Liao, X. Yan, Y. Yang, J. Wang, C. Chang, Q. Chu, Z. Deng, B. Lu, M. Liu, et al., Effects of heat treatment on the microstructures and magnetic properties of selective laser melted Fe-3 wtsoft magnet, J. Alloys Compd. 951 (2023) 169840.
[2] G. Stornelli, A. Faba, A. Di Schino, P. Folgarait, M.R. Ridolfi, E. Cardelli, R. Montanari, Properties of additively manufactured electric steel powder cores with increased Si content, Materials 14 (6) (2021) 1489.
[3] Y. Kim, H. Lee, T. Ha, J. Kim, J.P. Choi, Effects of laser beam profiles on the microstructure and magnetic properties of L-PBF soft magnetic alloys, Sci. Rep. 15 (1) (2025) 22336.
[4] M. Biyiklioglu, C. Guerra, R. Setchi, P. Anderson, In-Situ alloying of high-silicon soft magnetic alloy in laser powder bed fusion, Progress Additive Manufact. 11 (2) (2026) 2151–2163.
[5] C. Backes, M. Kahlert, M. Vollmer, M. Smaga, T. Niendorf, T. Beck, Microstructure and magnetic domain structure of additively manufactured Fe–Si soft magnetic alloys with 3 and 9 wt.-% Si, J. Mater. Res. Technol. 29 (2024) 1691–1702.
[6] B. Li, W. Zhang, W. Fu, F. Xuan, Laser powder bed fusion (L-PBF) 3D printing thin overhang walls of permalloy for a modified honeycomb magnetic-shield structure, Thin-Walled Struct. 182 (2023) 110185.
[7] N. Sim, H.Y. Jung, K.-A. Lee, Characterization of the microstructural, magnetic, and thermal properties of Fe–45Ni fabricated by laser powder bed fusion, Sci. Rep. 16 (1) (2026) 8049.
[8] M.G. Özden, F.S. Freeman, N.A. Morley, Soft-Magnetic behavior of Fe-Based nanocrystalline alloys produced using laser powder bed fusion, Adv. Eng. Mater. 25 (19) (2023) 2300597.
[9] L. Thorsson, M. Unosson, X. Jin, P. Tiberto, G. Barrera, B. Adam, N. Neuber, A. Ghavimi, M. Frey, R. Busch, et al., Selective laser melting of a Fe-Si-Cr-BC-based complex-shaped amorphous soft-magnetic electric motor rotor with record dimensions, Mater. Design 215 (2022) 110483.

[10] C. Gao, J. Hu, X. Yao, H. Pan, C. Shuai, Competitive microstructural evolution on the soft magnetic and mechanical properties of FeSiB amorphous/nanocrystalline alloys fabricated by laser-beam powder bed fusion, J. Mater. Sci. Technol. 246 (2026) 28–43.
[11] P. Pathak, M.S. K. K.Y. Nartu, Additive manufacturing of soft magnetic high entropy alloys: a review, J. Magn. Magn. Mater. 627 (2025) 173148.
[12] A.D. Goodall, L. Chechik, F. Livera, I. Todd, Importance of surface roughness on the magnetic properties of additively manufactured FeSi thin walls, Acta Mater. 263 (2024) 119501.
[13] Z.-Y. Zhang, K.J. Jhong, C.-W. Cheng, P.-W. Huang, M.-C. Tsai, W.-H. Lee, Metal 3D printing of synchronous reluctance motor, in: 2016 IEEE International Conference on Industrial Technology (ICIT), IEEE, 2016, pp. 1125–1128.
[14] G.-M. Tseng, K.-J. Jhong, M.-C. Tsai, P.-W. Huang, W.-H. Lee, Application of additive manufacturing for low torque ripple of 6/4 switched reluctance motor, in: 2016 19Th International Conference on Electrical Machines and Systems (ICEMS), IEEE, 2016, pp. 1–4.
[15] A. Elaskri, A. Ellery, 3D Printed electric motors as a step towards self-replicating machines, in: Proc Int Symp Artificial Intelligence, Robotics and Automation in Space, 2020.
[16] L. Kučerová, A. Benediktová, K. Burdová, D. Jandová, Low-temperature precipitation strengthening of maraging steel 1.2709 produced by powder bed fusion, Mater. Des. 241 (2024) 112938.
[17] J. Bochnia, T. Kozior, J. Zyz, The mechanical properties of direct metal laser sintered thin-walled maraging steel (MS1) elements, Materials 16 (13) (2023) 4699.
[18] A.R. de Oliveira, V.F. de Oliveira, J.C. Teixeira, E.G. Del Conte, Investigation of the build orientation effect on magnetic properties and barkhausen noise of additively manufactured maraging steel 300, Addit. Manuf. 38 (2021) 101827.
[19] G.V. Thotakura, R. Goswami, T.V. Jayaraman, Evaluation of structure and magnetic properties of maraging steel powder feedstock for additive manufacturing of magnetic components, J. Alloys Compd. 814 (2020) 152296.
[20] T. Aho, V. Sihvo, J. Nerg, J. Pyrhonen, Rotor materials for medium-speed solid-rotor induction motors, in: 2007 IEEE International Electric Machines & Drives Conference, 1, IEEE, 2007, pp. 525–530.
[21] M. Ma, X. Zhao, X. Sun, J. Jiang, W. Shao, L. Zhen, Microstructure evolution and strengthening mechanism of Feco-1.5 V0. 5Nb0. 4w soft magnetic alloy rolled strip with high yield strength and low coercivity, Acta Mater. 268 (2024) 119793.
[22] T. Dobeneck, A systematic analysis of natural magnetic mineral assemblages based on modelling hysteresis loops with coercivity-related hyperbolic basis functions, Geophys. J. Int. 124 (3) (1996) 675–694.
[23] M. Jackson, P. Solheid, On the quantitative analysis and evaluation of magnetic hysteresis data, Geochem. Geophys. Geosyst. 11 (4) (2010).
[24] S. Steentjes, M. Petrun, G. Glehn, D. Dolinar, K. Hameyer, Suitability of the double langevin function for description of anhysteretic magnetization curves in NO and GO electrical steel grades, AIP Adv. 7 (5) (2017).
[25] L.D. Domenig, K. Roppert, M. Kaltenbacher, Incorporation of a 3-D energy-based vector hysteresis model into the finite element method using a reduced scalar potential formulation, IEEE Trans. Magn. 60 (6) (2024) 1–8.
[26] R. Chen, F. Martin, Y. Li, S. Yue, A. Belahcen, An energy-based anisotropic vector hysteresis model for rotational electromagnetic core loss, IEEE Trans. Ind. Electron. 71 (6) (2023) 6084–6094.
[27] F.J.G. Landgraf, M. Emura, M.F. De Campos, On the steinmetz hysteresis law, J. Magn. Magn. Mater. 320 (20) (2008) e531–e534.
[28] H. Tiismus, A. Kallaste, A. Belahcen, M. Tarraste, T. Vaimann, A. Rassõlkin, B. Asad, P. Shams Ghahfarokhi, AC Magnetic loss reduction of SLM processed Fe-Si for additive manufacturing of electrical machines, Energies 14 (5) (2021) 1241.
[29] F. Habiby, A. Ul Haq, A.Q. Khan, Influence of austenite on the coercive force, electrical resistivity and hardness of 18% ni maraging steels, Mater. Des. 13 (5) (1992) 259–264.
[30] A.Z. Macknojia, J.V. Tran, M.P. Mckinstry, J. Galindo, Y. Jin, S. Dowden, S.M. Patil, M.V. Pantawane, K.V.M. Krishna, R. Banerjee, et al., Additive manufacturing of Fe-6.5 wt.% si transformer steel toroidal cores: process optimization, design aspects, and performance, Mater. Des. 241 (2024) 112883.
[31] A. Selema, M. Beretta, J. Verwimp, M. Rombouts, M.N. Ibrahim, K.B. Tawfiq, J. Vleugels, H. Vansompel, P. Sergeant, New measurement approach and development of 3-D-Printed core for yokeless axial-Flux machine, IEEE Sens. J. 24 (12) (2024) 18986–18999.
[32] B. Koo, M.-S. Jang, Y.G. Nam, S. Yang, J. Yu, Y.H. Park, J.W. Jeong, Structurally-layered soft magnetic Fe-Si components with surface insulation prepared by shell-shaping selective laser melting, Appl. Surf. Sci. 553 (2021) 149510.
[33] H. Tiismus, A. Kallaste, A. Belahcen, A. Rassolkin, T. Vaimann, P. Shams Ghahfarokhi, Additive manufacturing and performance of E-type transformer core, Energies 14 (11) (2021) 3278.
[34] D. Goll, D. Schuller, G. Martinek, T. Kunert, J. Schurr, C. Sinz, T. Schubert, T. Bernthaler, H. Riegel, G. Schneider, Additive manufacturing of soft magnetic materials and components, Addit. Manuf. 27 (2019) 428–439.
[35] B. Kocsis, I. Hatos, L.K. Varga, 3D Printed metal-insulator layered structure, J. Magn. Magn. Mater. 563 (2022) 169994.
[36] A.D. Goodall, G. Yiannakou, L. Chechik, R.L. Mitchell, G.W. Jewell, I. Todd, Geometrical control of eddy currents in additively manufactured Fe-Si, Mater. Des. 230 (2023) 112002.
[37] A. Plotkowski, J. Pries, F. List, P. Nandwana, B. Stump, K. Carver, R.R. Dehoff, Influence of scan pattern and geometry on the microstructure and soft-magnetic performance of additively manufactured Fe-Si, Addit. Manuf. 29 (2019) 100781.
[38] A.D. Goodall, L. Chechik, R.L. Mitchell, G.W. Jewell, I. Todd, Cracking of soft magnetic FeSi to reduce eddy current losses in stator cores, Addit. Manuf. 70 (2023) 103555.
[39] K. Monkova, I. Zetkova, L. Kučerová, M. Zetek, P. Monka, M. Daňa, Study of 3D printing direction and effects of heat treatment on mechanical properties of MS1 maraging steel, Archive Appl. Mech. 89 (5) (2019) 791–804.
[40] L. Kučerová, K. Burdova, V. Marková, J. Zálabskỳ, M. Ťavodová, Using the design of experiments methodology to evaluate the heat treatment of additively manufactured maraging steel, J. Mater. Res. Technol. 26 (2023) 8688–8703.
[41] J. Kaska, D. Pánek, Topological optimization for loss reduction in additively manufactured soft magnetic materials, IEEE Trans. Magn. (2025).
[42] Z. Frank, J. Laksar, Detection of interturn short-Circuits of E-Bike BLDC motor, in: IECON 2021–47Th Annual Conference of the IEEE Industrial Electronics Society, IEEE, 2021, pp. 1–6.
[43] Z. Frank, J. Laksar, K. Hruska, Overloadability improvement of electric motorcycle edrive by using a five-phase PMSM, Electr. Eng. (2025) 1–13.